LASER INTERFEROMETER GRAVITATIONAL WAVE OBSERVATORY
- LIGO -
CALIFORNIA INSTITUTE OF TECHNOLOGY
MASSACHUSETTS INSTITUTE OF TECHNOLOGY

| **Technical Note** | **LIGO-T010075-01-I** | 2008/04/01 |
|---|---|---|

# Advanced LIGO Systems Design

Avanced LIGO Systems Group, P. Fritschel, ed.

*Distribution of this document:*

Systems PDR Committee

This is an internal working
note of the LIGO project

**California Institute of Technology**
**LIGO Project, MS 18-34**
**Pasadena, CA 91125**
Phone (626) 395-2129
Fax (626) 304-9834
E-mail: info@ligo.caltech.edu

**Massachusetts Institute of Technology**
**LIGO Project, Room NW22-295**
**Cambridge, MA 02139**
Phone (617) 253-4824
Fax (617) 253-7014
E-mail: info@ligo.mit.edu

**LIGO Hanford Observatory**
**Route 10, Mile Marker 2**
**Richland, WA 99352**
Phone (509) 372-8106
Fax (509) 372-8137
E-mail: info@ligo.caltech.edu

**LIGO Livingston Observatory**
**19100 LIGO Lane**
**Livingston, LA 70754**
Phone (225) 686-3100
Fax (225) 686-7189
E-mail: info@ligo.caltech.edu

http://www.ligo.caltech.edu/

# 1 Introduction

Advanced LIGO will replace the three initial LIGO interferometers with three interferometers using new hardware for each interferometer subsystem. The new instruments are designed to provide approximately an order of magnitude better gravitational wave strain sensivity, and over a wider frequency band. In addition, the arm length of LHO's H2 interferometer will be increased from 2 km to 4 km, so that all three interferometers could in principle be operated with the same strain sensitivity.

This document describes the system design and requirements for the Advanced LIGO detectors. This version has been prepared for the Advanced LIGO Systems Preliminary Design Review (March-April 2008), and is a major update from the original version (v. 00, June 2001).

# 2 System Level Requirements

## 2.1 Strain Noise

The goal sensitivity for the Advanced LIGO detectors is defined in Refs. [1] and [2] as: an equivalent (single interferometer) strain noise of $10^{-22}$ RMS, integrated over a 100 Hz bandwidth centered at the minimum noise region of the strain spectral density.

## 2.2 Non-Gaussian Noise

The initial LIGO science requirements document ([3]) specified that, at the targeted threshold of sensitivity, the false signal rate (i.e., triple coincidences not due to astrophysical sources) should be held to less than 0.1 events per year. For Advanced LIGO, we would like to reach a rate at least as low as this, if not lower. However, there are few if any places where this can really be quantitatively factored into the hardware design. Lessons learned from initial LIGO about potential sources of glitches must be taken into account. In addition, general mechanical design rules are followed, such as limiting stress concentrations and avoiding bolts in sensitive locations.

## 2.3 Availability

The detector availability goals for initial LIGO are also adopted for Advanced LIGO; these are [3]:

- Single interferometer operation: 90% availability (annually integrated), minimun lock duration of 40 hours
- Double coincidence operation (LLO interferometer with either LHO interferometer): 85% availability, averaged annually
- Triple coincidence operation: 75% availability, averaged annually

For comparison, the corresponding duty cycles over the last 30 days of initial LIGO's S5 run were: 88%, 85.2% and 76.3% for H1, H2 and L1 single operation, respectively; 73.8% for LLO-LHO double coincidence; 69.1% for triple coincidence. These numbers represent significant improvement over the course of the run; the duty cycles averaged over all S5 are 10-15% lower than these.

### 2.4 Environmental Sensing

The detector environment will be monitored with initial LIGO's Physics Environment Monitoring (PEM) system. No additional monitoring functions are planned at this time. A future PEM upgrade might involve deploying more vibration sensors for the ground and vacuum equipment, for the purpose of subtraction of Newtonian noise from the data stream.

### 2.5 Calibration and Data Acquisition

The effects of calibration uncertainty were considered for initial LIGO in Ref. [4]. The conclusions of this analysis remain valid, and establish the calibration accuracy goal for Advanced LIGO: strain amplitude calibration accuracy, $\pm 2\%$; absolute timing uncertainty (determination of gravitational-wave arrival time in the infinite signa-to-noise ration limit), $\pm 10\,\mu$sec.

The gravitational-wave data channel(s) will be recorded at a rate of 16384 samples/sec (same as initial LIGO), with a bandwidth of 7400 Hz or greater and a precision sufficient for the dynamic range of the channel. Collaborative channels that monitor the instrument (dozens of non-GW degrees-of-freedom) and its environment (the PEM subsystem) will also be recorded so that they can be used to distinguish instrumental artifacts from potential GW signals.

## 3 System Design

The Advanced LIGO configuration, shown in Figure 1, is a Michelson interferometer with Fabry-Perot arms cavities, and both power recycling and signal recycling (i.e., the initial LIGO configuration, with the addition of signal recycling). There is both an input mode cleaner (as in initial LIGO) and output mode cleaner (new with Advanced LIGO), the latter being required for the gravitational wave (GW) readout. Top level design parameters are given in Table 1.

### 3.1 Modes of operation

Two features of the interferometer design provide flexibility so that, unlike initial LIGO, the detectors can be operated in different modes with good broadband GW sensitivity, or sensitivity targeted to specific frequency bands. The two features are: tuning of the signal recycling cavity (SRC); the trade-off between low frequency and high frequency noise with laser power.

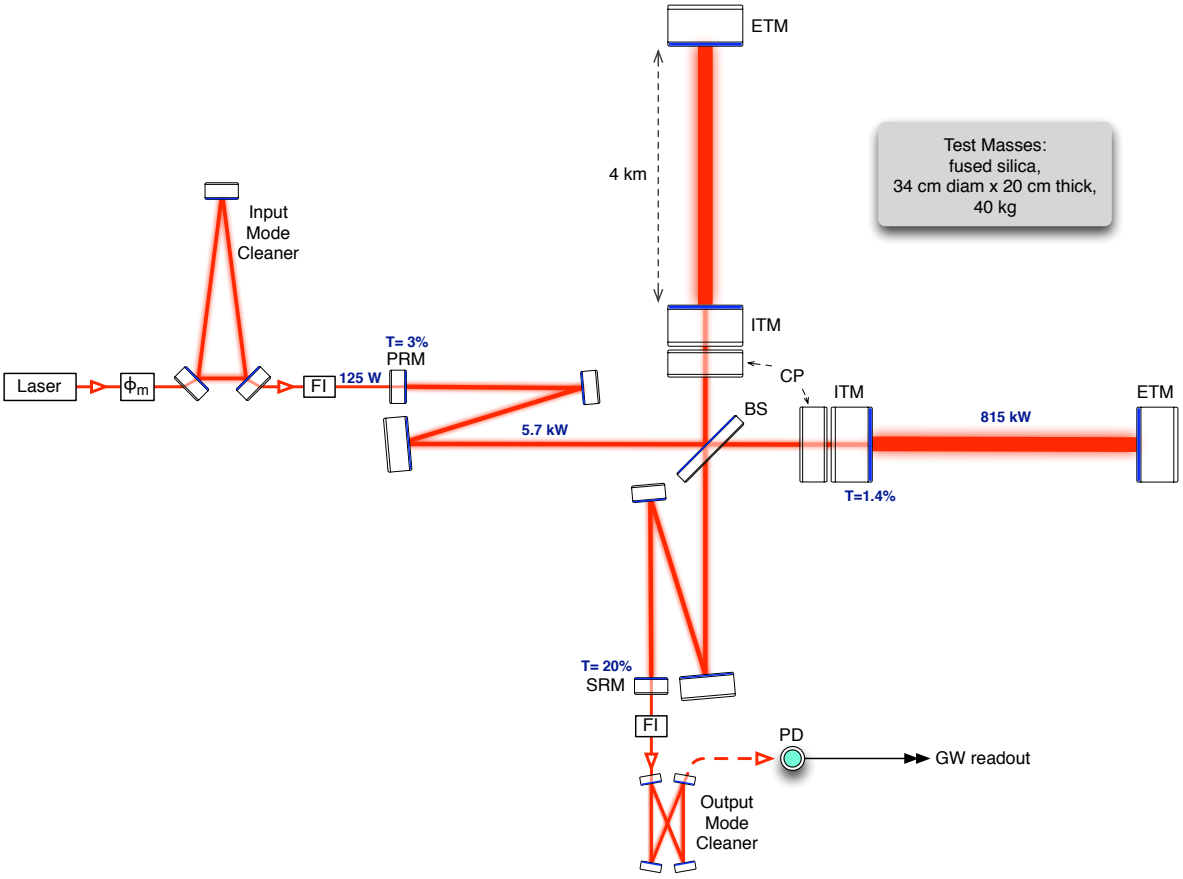


Figure 1: Advanced LIGO interferometer configuration. ETM, end test mass; ITM, input test mass; BS, 50/50 beamsplitter; CP, compensation plate; PRM, power recycling mirror; SRM, signal recycling mirror; FI, Faraday isolator; $\phi_{\rm m}$, phase modulation; PD, photodetector. The power levels shown correspond to full-power operation; the interferometers can also be operated at much lower powers with good strain sensitivity.

| *Parameter* | *Value* | *Comments* |
|---|---|---|
| Arm length | 3995 m | |
| Arm cavity finesse | 450 | see Sec. 3.6 |
| Laser type and wavelength | Nd:YAG, $\lambda = 1064\,\mathrm{nm}$ | |
| Max. input power (@ PRM) | 125 W | |
| Test mass material | Fused silica | see Sec. 3.7 |
| Test mass size & mass | $\phi 34\,\mathrm{cm} \times 20\,\mathrm{cm}$, 40 kg | see Sec. 3.8 |
| Beam radius ($1/e^2$), ITM / ETM | 5.55 cm / 6.2 cm | see Sec. 3.4 |
| Radii of curvature, ITM / ETM | 1970 m / 2192 m | see Sec. 3.5 |
| Beamsplitter size & mass | $\phi 37\,\mathrm{cm} \times 6\,\mathrm{cm}$, 14 kg | |
| Michelson (Schnupp) asymmetry | 5 cm | see LIGO-T070247-00 |

Table 1: Parameters of the Advanced LIGO interferometers. Arm lengths are approximate only; exact values are found in Ref. [5]. For a complete list of optics dimensions and parameters see Ref. [6].

Advanced LIGO's sensitivity improvement at frequencies below $\sim 200\,Hz$ are mostly the result of the much better seismic isolation and test mass suspensions. We propose to capitalize on these hardware improvements as rapidly as possible by taking a staged approach to the interferometry. The approach that currently appears most attractive is to begin operating the interferometer without signal recycling, and at a modest power level. Broadband signal recycling is then introduced, again at a modest power level to begin with. The operating power would then be increased in the broadband mode, up to the maximum power available depending on the frequency band one wants to target, and the difficulties handling high power. Tuned operation of the signal cavity could follow (e.g., optimized for binary neutron star inspiral), as informed by results.

Strain noise spectra for these modes are shown in Fig. 2 and operating parameters are given in Table 2.

**mode 0** In this mode there is no signal recycling (SRM transmission of 100%), and modest input power (25 W). Since this configuration is so similar to the initial LIGO interferometer, we would expect to be able to get running in this mode fairly quickly, and start taking data with significantly better sensitivity than initial LIGO.

**mode 1** In this mode there is broadband signal recycling (i.e., zero detuning of the signal recycling cavity). This mode is expected to be significantly easier to control than those where the signal cavity is tuned away from zero frequency. This could be run at different input powers (the spectra for two are shown below), starting with low power. At high power, the sensitivity to binary neutron star inspirals is almost as good as can be achieved by specifically tuning for them.

**mode 2** This is the canonical mode with full power and the SRC tuned to optimize sensitivity to NS-NS inspirals. We have however fixed the SRM transmission at 20%,

which is a bit higher than the optimum for NS-NS sensitivity, as a compromise with the broadband case (the difference is less than 0.4%).

**mode 3** This mode optimizes for 30-30 solar mass binary black hole inspirals, with a fixed SRC detuning of 20 degrees and SRM transmission of 20%.

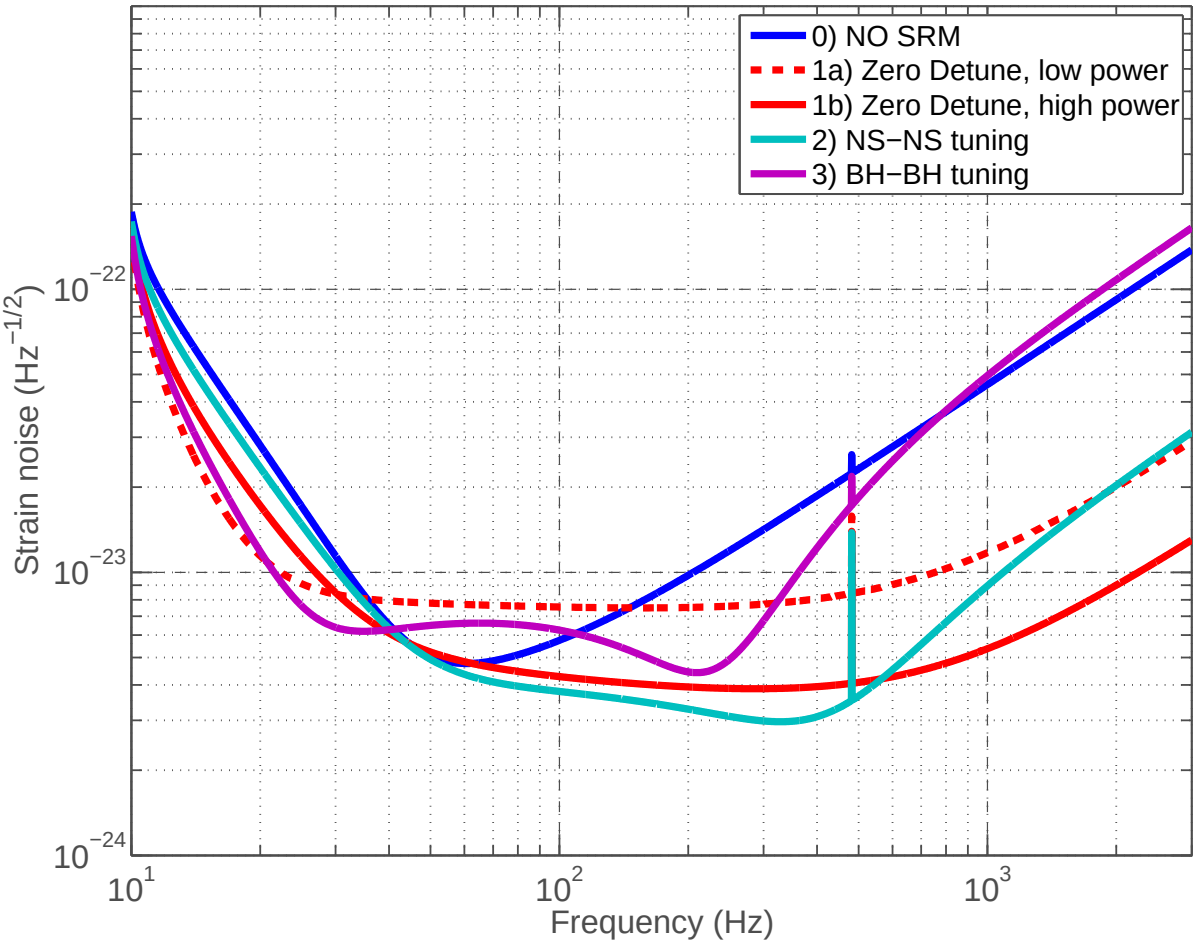


Figure 2: Proposed modes of operation for the Advanced LIGO interferometers. See text for description of the modes.

## 3.2 Signal Recycling

Signal recycling is included in the design because it offers advantages in sensitivity and in practical operations. For the maximum input and stored arm powers, a non-signal recycled interferometer could in principle reach a NS-NS inspiral range that is only about 10% lower than the signal-recycled version, but the power recycling cavity (PRC) would need to support about 10 times more power in this case and the losses in the PRC would need to be kept extremely low. And of course signal recycling is needed to really optimize sensitivity above a couple of hundred Hertz.

| *Mode* | *NS-NS Range* | *BH-BH Range* | $P_{in}$ | $T_{SRM}$ | $\phi_{SRC}$ | $h_{\rm RMS}$, $10^{-22}$ (band) |
|---|---|---|---|---|---|---|
| 0 | 143 Mpc | 1.28 Gpc | 25 W | 100% | – | 0.57 (40–140 Hz) |
| 1a | 145 Mpc | 1.48 Gpc | 25 W | 20% | 0 deg. | 0.75 (120–220 Hz) |
| 1b | 180 Mpc | 1.32 Gpc | 125 W | 20% | 0 deg. | 0.39 (265–365 Hz) |
| 2 | 186 Mpc | 1.13 Gpc | 125 W | 20% | 11 deg. | 0.30 (285–385 Hz) |
| 3 | 170 Mpc | 1.68 Gpc | 20 W | 20% | 20 deg. | 0.47 (155–255 Hz) |

Table 2: Sensitivities for the operational modes described above, and shown in Fig. 2; the last column gives the minimum RMS strain noise in a 100 Hz band.

The Advanced LIGO interferometer will be built at least initially with fixed-transmission signal recycling mirrors (SRM). This means that to achieve the best narrow-band sensitivity above $\sim 1$ kHz, the SRM would need to be changed for one with a lower transmission. A later uprade could implement a variable-transmission SRM.

### 3.3 GW Channel Readout

Readout of the gravitational-wave channel will be done using an output mode cleaner in conjunction with homodyne, or DC, detection. This is a major departure from the initial LIGO readout, however the new scheme is currently being implemented for Enhanced LIGO.

The output mode cleaner will filter out non-$\rm TEM_{00}$ mode carrier power, and any power in RF modulation sidebands, so that only the carrier $\rm TEM_{00}$ mode power is detected. This greatly reduces the power on the detectors, lowering the noise with only a small reduction in signal.

Homodyne (DC) readout was adopted over heterodyne (RF) readoud in 2003 ([7]) due to its intrinsically lower sensing noise and reduced sensitivity to laser and technical noises. The sensing noise comparison between the two types of readout is made in Ref. [8], and a recent review of technical considerations, including comparison data from the 40m interferometer, can be found in Ref. [9].

### 3.4 Beam Sizes

The beam sizes on the test masses will be 5.55 cm on the ITMs and 6.20 cm on the ETMs ($1/e^2$ intensity radius). They are made large (compared to initial LIGO) in order to reduce test mass thermal noise by averaging over more of the mirror surface. The dominant noise mechanism here is mechanical loss in the dielectric mirror coatings, for which the displacement (amplitude) noise scales as 1/(beamsize). Close behind is thermo-optic noise in the coatings, which scales as $(\text{beamsize})^{-1/2}$.

The thermal noise reduction with increased beam size has to be balanced against increased aperture loss and decreased mode stability. Until recently the beam sizes were taken to be the same on all test masses (6.0 cm). The new asymmetric design takes advantage of the fact that the ETMs are more important for reducing thermal noise because their coatings

are thicker (2-3 times as thick as the ITMs). Therefore we can achieve the essentially the same level of thermal noise and mode stability by making the beam larger on the ETM and smaller on the ITM. This has the advantage of reducing aperture loss in the beamsplitter and recycling cavities. For a quantitative comparison of the symmetric and asymmetric designs, see Ref. [10].

The chosen design has fairly low aperture loss in the arms, 2–3 ppm on the ETMs. While this could arguably be allowed to be larger, doing so would push the arm cavities further toward the mode stability edge (the design has $g_1 g_2 = 0.845$, where the stable zone is $0 \leq g_1 g_2 \leq 1$). Tighter tolerances would be needed on the arm mirror radii of curvature; larger-scale polishing distortions would become important. We are therfore reluctant to go further in this direction without having some experience making and operating cavities in this regime.

### 3.5 Arm Cavity Radii of Curvature

The chosen mirror beam sizes can be achieved with either of two designs: a nearly-planar cavity or a nearly-concentric one. Our choice is made from consideration of optical torques in the arm cavities, which become important at the Advanced LIGO power levels. The analysis of optical torques given in Ref. [11] shows that there is a preference for the nearly concentric design. In this case, the torsional mode with the higher optical stiffness is statically stable, whereas it would be statically unstable for a near planar design.

The near-concentric design has a smaller arm cavity waist ($\omega_0 = 1.3$ cm) by a factor of 3.5. This does lead to larger phase noise from beam tube residual gas fluctuations, but this is still a small noise term. We're not aware of any other disadvantages of the smaller waist.

### 3.6 Arm Cavity Finesse

With signal recycling, the quantum noise-limited strain sensitivity is more-or-less independent of the arm cavity finesse, and the finesse choice is guided by practical considerations. Generally these argue for a higher arm cavity finesse than in initial LIGO. Historically the Advanced LIGO arm finesse has been 1200, increased by nearly a factor of 6 from initial LIGO in order to limit the laser power in the Michelson optic substrates.

Recently the issue of arm finesse has been more carefully analyzed, taking into account the application of ultra-low absorption fused silica for critical core optics. This analysis, found in Ref. [12], led to a new arm finesse value of 450.

### 3.7 Test Mass Material

The test masses will be made of fused silica. This is a change from version-00 of this document (June 2001), where sapphire was considered the baseline and fused silica a viable fallback. The pros and cons of the two materials were examined in the ensuing years, and at the end of 2004 an evaluation committee concluded that fused silica was the better choice. This decision is summarized in Ref. [13], and further technical details can be found in Ref. [14].

There are several types and grades of fused silica from which to choose. Low mechanical dissipation is of course important, but all types of fused silica are believed to have sufficiently low loss that this is not a criterion. For the input test masses, the important property is optical absorption. Initial LIGO uses a low-absorption grade (Heraeus 312), which has 3-4 ppm/cm of absorption at 1064 nm. Advanced LIGO will use the ultra-low-absorption Heraeus Suprasil 3001 material for the ITMs, for which the absorption is $< 0.5$ ppm. This will ensure that the power absorbed in the bulk is negligible compared to that absorbed in the coatings.

### 3.8 Test Mass Size

The mass of the fused silica test masses is 40 kg, four times larger than in initial LIGO. This (40 kg) was the maximum available for sapphire, but is still smaller than the maximum fused silica piece available from Heraeus, which is 75-80 kg. While this yet larger mass could reduce radiation pressure noise below 30-40 Hz, it is too late in the design process to increase the mass (it is principally the test mass suspensions that would need to be redesigned).

The choice of aspect ratio is explored in Ref. [15]. It should be noted that while this considers thermal noise of the substrate as a function of aspect ratio, the dominant noise due to the optical coatings is not treated, as there is not yet a coating noise model that includes the finite test mass size.

### 3.9 Interferometer Optical Losses

Optical loss in the arms limits the power build-up and thus the shot-noise sensitivity, for a given input power. The goal for round-trip arm cavity loss is 75 ppm (includes scatter and absorption, and ETM transmission). This is a factor of 1.5-2 times lower than observed in the initial LIGO arm cavity mirrors.

The goal for round-trip loss in the power recycling cavity (not including the arms) is 1000 ppm, which corresponds to 5% of the loss from the arm cavities ($4 \cdot 75\,\text{ppm}/T_{\text{ITM}} = 2.1\%$). For the signal recycling cavity, the round-trip loss goal is 2000 ppm, 1% of the SRM transmission. The effect of this loss is shown in Appendix A.

### 3.10 Recycling Cavity Geometry

Both power- and signal-recycling cavities are made to be stable for the fundamental Gaussian modes they support. By *stable* we mean that the fundamental mode of the cavity accrues a non-negligible Gouy phase in a one-way propagation through the cavity. In contrast, the initial LIGO power recycling cavity is marginally stable, since the Gouy phase accumulation is very close to zero.

The pros and cons of both designs (stable and marginally-stable) have been considered and investigated. These will be described in a future technical note on the subject. The primary feature favoring the stable design is greater tolerance to distortions or defects in the optics. A modal model treatment of some of these effects can be found in Ref. [16].

### 3.11 Seismic Isolation

The main interferometer optics and components are mounted on in-vacuum, seismically isolated platforms (all components shown in Fig. 1, except the laser and phase modulators, are mounted on such platforms). Isolation from ground vibrations is achieved primarily by active stabilization, using low-noise sensors and force actuators, providing suppression in roughly the band from 0.1 Hz to 10-30 Hz. There are two layers of isolation:

- Hydraulic external pre-isolators (HEPI). These isolators are external to the vacuum system, and use low-noise hydraulic actuators for control in six degrees-of-freedom. This stage also provides positioning control of the optics platform, with a range of approximately 1 mm. (HEPI isolators have been installed on the LLO interferometer since 2003.)
- Internal seismic isolators (ISI). This layer is inside the vacuum chambers, and uses electro-magnetic actuators for control. For the optics platforms in the BSC chambers, there are two such stages cascaded in series, each of which is controlled in six degrees-of-freedom (DOF). For the platforms in HAM chambers, there is a single, six DOF stage.

With two ISI stages, better isolation is provided for the test masses and beamsplitter (the optics that occupy BSC chambers). Until roughly two years ago, the same two-stage ISI design was carried for the HAM platforms as well. The isolation needs for the auxiliary optics mounted on these platforms was more closely investigated in 2006 ([17]), and this led to relaxation of the isolation requirements. The single-stage design for the HAM platform was then adopted ([18]), as a worthy trade-off of performance for simplicity.

### 3.12 Suspensions

Most of the in-vacuum interferometer optics and components are mounted in pendulum suspensions, which are in turn mounted to the seismic optics platforms. The suspension designs vary, depending on performance needs and physical constraints; most are multi-stage suspensions for better isolation compared to the initial LIGO, single-stage design. In addition, the test mass suspensions include a suspended reaction mass chain adjacent to the main chain, as low-noise points from which control forces can be applied to the main chain. Here is a summary of the different suspension types:

### 3.13 Thermal Effects and Compensation

As in initial LIGO, the interferometers will include active thermal compensation (though this time it is designed in from the beginning). The scheme used for initial LIGO, however, where a compensating $CO_2$ laser beam shines on the high-reflectivity side of the ITMs, does not scale well to Advanced LIGO. Furthermore, it is not just substrate thermal lensing that must be compensated. With the higher powers and near-concentric arm cavities of Advanced LIGO, thermo-elastic deformation of the test mass surfaces becomes significant.

| *Component* | *No. of stages* | *Fiber type* | *Reaction mass?* |
|---|---|---|---|
| Test masses | 4 | fused silica | yes |
| Beamsplitter | 3 | steel wire | no |
| Fold mirrors | 3 | steel wire | no |
| Recycling cavity optics | 3 | steel wire | no |
| Input mode cleaner mirrors | 3 | steel wire | no |
| Output mode cleaner | 2 | steel wire | no |
| Output Faraday isolation | 1 | steel wire | no |
| ETM transmission monitor | 1 | steel wire | no |

Table 3: Summary of suspension types in the interferometer. *Fiber type* refers to the fiber at the last stage of the suspension, supporting the optic. The compensation plate is not listed because it is the reaction mass for the ITM suspension.

The compensation scheme is therefore significantly different: a radiative ring heater will surround each test mass, and a compensation plate is included in each arm of the Michelson, suspended between the beamsplitter and each ITM. The test mass ring heaters can maintain the radii of curvature constant (keeping the cavity mode constant). The compensation plates are actuated on with $CO_2$ laser beams to compensate thermal lensing, with the advantage of being less sensitive to actuator laser noise than with direct test mass actuation.

### 3.14 Parametric Instabilities

Opto-mechanical parametric couplings in the arm cavities have the potential to lead to unstable build-up of such coupled, higher-order modes. Unchecked, the mechanism would impose a limit on the power stored in the arms. The mechanical side of the effect involves acoustic modes of the test masses; the optical side involves higher-order spatial eigenmodes of the arm cavities. Under certain conditions, the two types of modes can non-linearly feed energy into each other, removing it from the main carrier mode.

The signifigance of the effect was first recognized by the Braginsky group [19], and the first detailed analyses for Advanced LIGO cavities were done by the University of Western Australia group [20],[21]. The general conclusion of these and other analyses (see in particular Refs. [22] and [23]), is that there may be 5-10 modes per test mass that could become unstable (note though that current calculations have all been done using the obsolete arm finesse of 1200, three times higher than new design).

Several methods of mitigating parametric instabilities have been suggested: selected application of mechanically lossy material on the test mass barrel; active mode damping via the electro-static actuators, or through radiation pressure from additional laser beams; reduction of optical gain by restricting the test mass apertures. None of these are currently part of the baseline design, however, this remains an active area of investigation, and some mitigation method may be adopted in the future.

### 3.15 Arm Length Stabilizer

Extrapolating from initial LIGO, one concludes that lock acquisition of the interferometers presents a dicey situation. While the active seismic isolation system for Advanced LIGO provides substantial ground noise suppression at frequencies above about 0.5 Hz, lower frequency fluctuations, which dominate the rms arm length variation, are not expected to be significantly smaller than in initial LIGO. Furthermore, the maximum acceleration that can be applied to the test mass ($F/M = 5\mu\text{m/sec}^2$) is much smaller than in initial LIGO ($3\text{mm/sec}^2$), and the cavity linewidth is twice as narrow.

The acquisition problem could be greatly simplified by a system that would stabilize the arm lengths, independently of the interferometer global control. Several schemes have been envisioned for doing this, known by the names Seismic Platform Interferometer (SPI) and Lock Acquisition Interferometer (LAI) [24]. The goal for such an arm length stabilization is to be able to control the length of each arm to a determined length (relative to a resonance for the main beam, and typically a few linewidths away from a main beam resonance), with residual fluctuations of order 1 nanometer.

We are including a 'placeholder' in the systems design for some implementation of such a stabilization system. Three specific schemes that have been proposed over the past year all appear to be feasible, with the potential to reach the stabilization goal. We have not yet determined which scheme to adopt. A technical report on all the schemes is being prepared by the group at Australia National University, and will be reviewed by Advanced LIGO Systems to determine which course to take (this should occur by summer 2008).

# 4 System Level Noise Sources

## 4.1 Fundamental noise sources

The interferometer noise floor is designed to be limited by fundamental noise source – quantum noise and thermal noise. While these arise from fundamental physical mechanisms and cannot be 'engineered away', they depend on parameters that can be controlled to some degree. This section shows the equivalent strain noise due to these sources, and describes the current parameter values that are used in the calculations.

### 4.1.1 Quantum noise

For a given stored power in the arm cavities, the quantum noise spectrum is affected in detail by the signal recycling mirror reflectivity, loss in the signal recycling cavity, and the photodetector quantum efficiency. Before December 2006, quantum noise was typically calculated using an approximate expression that did not properly account for losses in the signal cavity. Beginning with version 6, Bench uses the expressions that include loss, as found in Section V of Ref. [25].

The following values are used for the loss parameters: 90% for the photodetection efficiency (this accounts for finite transmission through the Faraday isolator and output mode cleaner, as well as photodetector quantum efficiency); 2000 ppm for the round-trip loss in the signal

recycling cavity. Figure 3 shows the quantum noise component for each of the modes described in Section 3.1. It also shows quantum noise for a high-frequency, narrowband mode, which requires a signal recycling mirror with a much smaller transmission (1.1%).

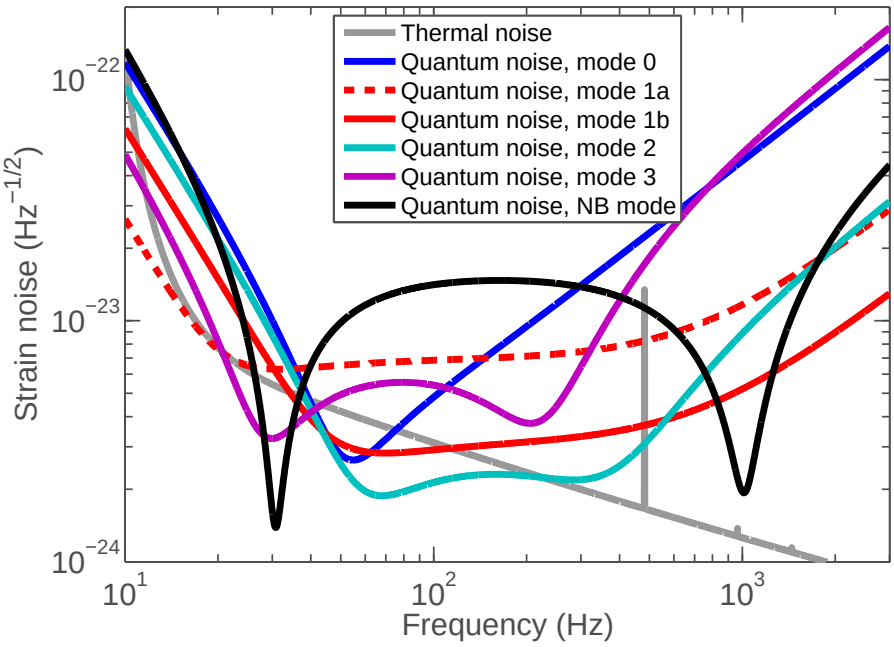


Figure 3: Quantum noise for the modes described in Section 3.1, and also a narrowband mode where the signal recycling mirror is changed for one with much smaller transmission (1.1% vs. 20%). Total thermal noise (suspension and test mass) is also shown for comparison.

### 4.1.2 Test mass internal thermal noise

The test mass internal thermal noise is calculated with the following components:

1. *Substrate Brownian noise.* Noise due to bulk mechanical loss is calculated according to Ref. [26], which includes finite size corrections. Surface loss is also included in the same way that coating loss is calculated. The bulk and surface loss model used in the calculation is that of Ref. [27].

2. *Substrate thermoelastic noise.* This is also calculated according to Ref. [26].

3. *Coating Brownian noise.* This is calculated according to the formulation in Ref. [28]. The main caveat is that the calculation does not account for the finite size of the test mass.

4. *Coating thermo-optic noise.* Coating thermoelastic noise is calculated according to Ref. [29], and thermorefractive noise according to Ref. [30]. These two noise terms are added coherently, to form the coating thermo-optic noise.

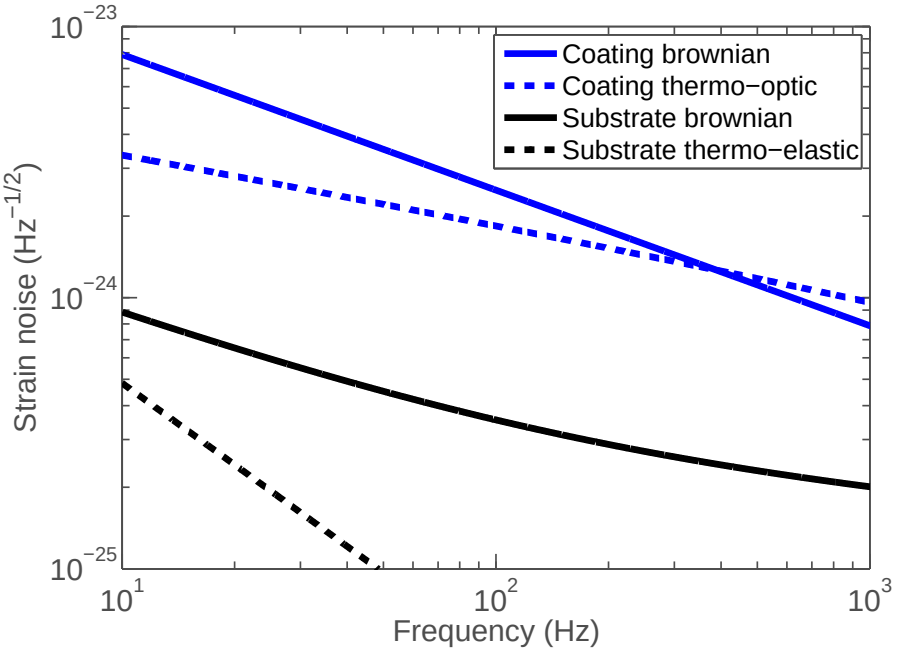


Figure 4: Strain noise due to test mass internal thermal noise. The coating contributions are calculated for the standard design of 1/4-wave layers.

TMcoatingComparison

| *Parameter* | *Value* |
|---|---|
| fused silica bulk loss | $7.6 \times 10^{-12} f^{0.77}$ |
| low-index coating material (silica) | |
| loss | $4 \times 10^{-5}$ |
| thermal expansion | $5.1 \times 10^{-7}/K$ |
| $dn/dT$ | $1.5 \times 10^{-5}/K$ |
| high-index coating material (doped tantala) | |
| loss | $2.3 \times 10^{-4}$ |
| thermal expansion | $3.6 \times 10^{-6}/K$ |
| $dn/dT$ | $6 \times 10^{-5}/K$ |
| optical transmission, ITM / ETM | 1.4% / 5 ppm |

Table 4: Significant parameters that determine the test mass internal thermal noise. There is still significant uncertainty in the tantala thermal parameters.

Strain noise from each component is shown in Fig. 4, calculated using the parameters in Table 4.

Coating noise is the dominant of these terms. The baseline coating design at present uses alternating layers of silica and tantalum pentoxide, in a standard design where the optical thickness of each layer is 1/4-wave. An alternative design is being pursued, where the same materials are used, but the layer thicknesses are altered to minimize thermal noise [31]. As shown below in Fig. 5, this coating design could reduce the noise by 10-15%.

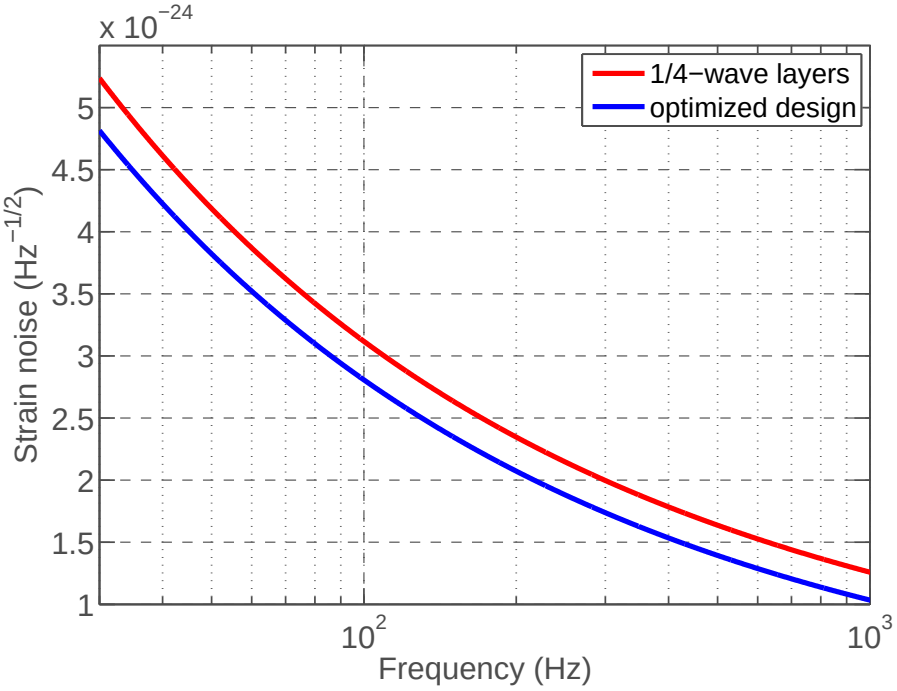


Figure 5: Strain noise from test mass internal thermal noise, for the standard 1/4-wave coating design, and the design which minimizes total thermal noise for the specified optical transmissions. Note that this is only representative of the type of improvement that could be made, since the specific design depends on some coating material parameters that are still uncertain.

### 4.1.3 Suspension thermal noise

A description of the calculation used for suspension thermal noise can be found in section 2.3 of Ref. [32]. It models the four stages of the suspension as point masses connected by springs. Dissipation in each stage is included as imaginary parts of the spring constants, including loss terms for bulk loss, surface loss, and thermoelastic damping. The thermal noise in the detection band is of course dominated by loss in the final suspension stage, which is calculated following Ref. [33].

The current baseline design for the last suspension stage uses four fused silica ribbons, with a 10:1 cross-section aspect ratio. Ribbon dimensions are chosen to achieve a vertical mode eigenfrequency below 10 Hz, and a fundamental violin mode frequency above 400 Hz. A

ribbon geometry gives lower loss than a uniform cross-section circular fiber that satisfies the same criteria.

It is very likely, however, that the baseline geometry will soon be changed to a circular fiber having a varying cross-section along its length. Such a geometry can achieve even lower loss than the ribbon while satisfying the eigenfrequency criteria, and is also easier to manufacture [34]. Thermal noise calculations for the baseline ribbon and the new circular design are shown in Fig. 6, and parameter values are given in Table 5.

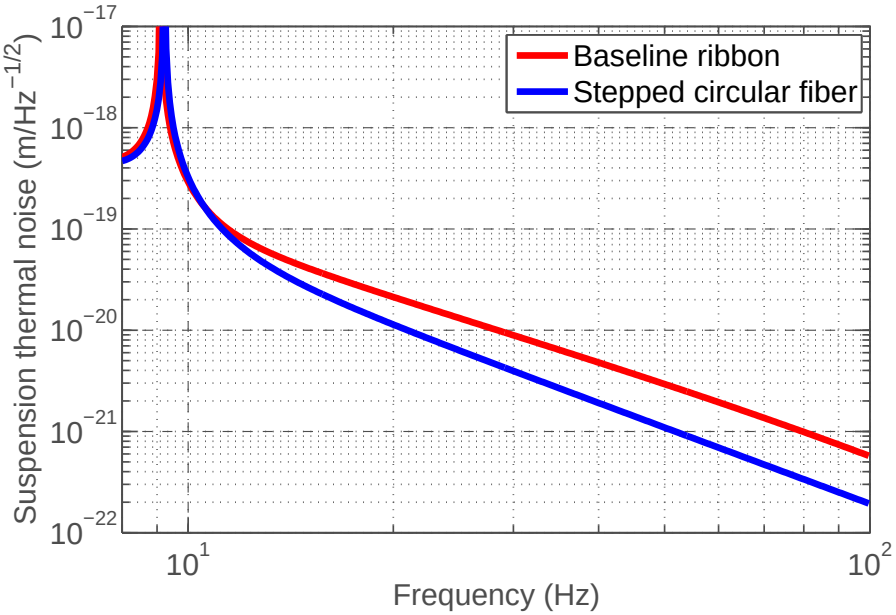


Figure 6: Suspension thermal noise (for a single test mass) for the baseline ribbon design and for a proposed circular fiber design, where the ends of the fiber are thicker than the middle. The traces include vertical thermal noise, with a cross-coupling factor of 0.001.

| *Parameter* | *Ribbon design* | *Optimized circular design* |
|---|---|---|
| Cross-section | 1.15 mm × 0.115 mm | $\phi 817\,\mu m$ (2.5 cm each end) |
| | | $\phi 410\,\mu m$ (middle 55.2 cm) |
| Heat capacity | 772 J/kg/°K | |
| Thermal conductivity | 1.38 W/m/kg | |
| Thermal expansion coeff. | $3.9 \times 10^{-7}$/°K | |
| Young's modulus ($E$) | $7.2 \times 10^{10}$ Pascals | |
| Temperature coeff. of $E$ | $dlnE/dT = 1.52 \times 10^{-4}$/°K | |
| Bulk mechanical loss | $4.1 \times 10^{-10}$ | |
| Dissipation depth | $1.5 \times 10^{-2}$ m | |

Table 5: Significant parameters of the test mass suspension glass fibers that determine suspension thermal noise.

## 4.2 Facility limits

### 4.2.1 Seismic gravity-gradient noise

Seismic waves produce density perturbations in the earth close to the test masses, which in turn produce fluctuating gravitational forces on the masses. This noise source is called seismic gravity-gradient noise, and is estimated using the transfer function formulation of Ref. [35]. This requires a model for the spectrum of rms seismic displacements averaged over vertical and horizontal directions ($W(f)$), and an estimate of a dimensionless reduced transfer function ($\beta$). We use a value of $\beta = 0.6$, compared to a total range found in Ref. [35] of $\beta = 0.15 - 1.4$. The model for $W(f)$ is shown in Fig. 7.

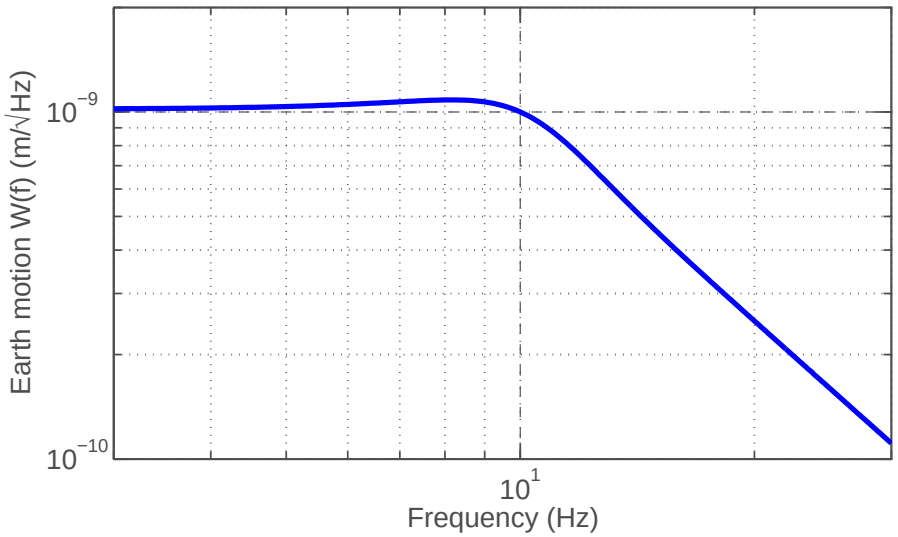


Figure 7: Model used for the rms seismic displacement in the gravity-gradient noise estimate, averaged over horizontal and vertical directions (the motion spectrum $W(f)$ as defined in Ref. [35]).

### 4.2.2 Residual gas noise

Optical path length noise due to residual gas in the beam tubes is calculated using the equation found in Ref. [36]. The calculation accounts for the changing beam size over the path along the arm. The noise curve includes only the dominant residual gas component, hydrogen, with a pressure of $4 \times 10^{-7}$ pascals (polarizability of $7.8 \times 10^{-31}\,\mathrm{m}^3$).

## 4.3 Technical noise sources

All technical noise sources are to be controlled so that the equivalent strain noise (amplitude spectral density) of each source is no more than 10% of the target strain sensitivity. This applies across the entire gravitational wave band ($10 - 7000\,\mathrm{Hz}$). Since the different operating modes have different strain noise floors, for guidance we form a technical noise floor by using the minimum strain noise amongst the modes at each frequency; this is shown in Fig. 8,

now displayed as equivalent differential-arm displacement noise. For some noise sources (particularly those that depend on power) this may be overly conservative; in these cases the technical noise limit can be calculated specifically for that situation.

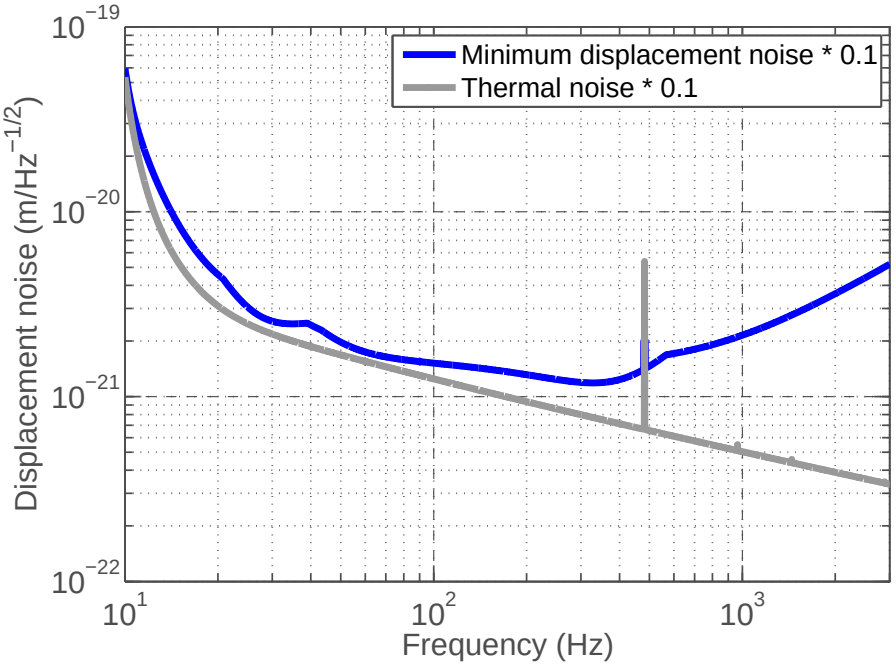


Figure 8: Equivalent differential-arm displacement noise limit for technical noise sources. The blue curve is 10% of the minima of the curves shown in Fig. 2 (converted to displacement by multiplying by the arm length). Displacement noise limit for a single test mass would be a factor of 2 smaller. For reference, the grey curve is 10% of the thermal noise (sum of suspension and test mass internal noise).

# 5 Subsystems

## 5.1 Prestabilized laser

The PSL subsystem includes:

- Nd:YAG laser, 1064 nm wavelength, single frequency, $TEM_{00}$ mode output power of 165 W.
- frequency prestabilization of the PSL output beam
- intensity stabilization of the input mode cleaner output beam
- frequency actuation inputs, for subsequent frequency control
- amplitude and frequency modulation inputs, for global diagnostics

The PSL design requirements are found in LIGO-T050036.

## 5.2 Seismic isolation

The seismic isolation subsystem includes:

- Hydraulic external pre-isolators (HEPI) for all BSC chambers, and all HAM chambers except HAM1 and HAM7.
- Single-stage active isolation platform for all HAM chambers, except HAM1 and HAM7.
- Two-stage active isolation platform for all BSC chambers.

General requirements for the seismic isolation system, and displacement noise requirements for the BSC platforms are found in LIGO-E990303. Displacement noise for the HAM platforms are found in LIGO-G060190.

## 5.3 Input optics

The input optics subsystem includes:

- electro-optic modulators for the interferometer sensing scheme
- input mode cleaner design
- mode matching elements between the input mode cleaner and the power recycling mirror
- cavity mode design for the power- and signal-recycling cavities (mirror radii of curvature and separations)
- power control of the beam incident on the input mode cleaner
- delivery of the interferometer reflected beam, the input mode cleaner reflected beam, and a sample of the IMC transmitted beam to detection ports
- Faraday isolator between the IMC and the power recycling mirror
- ensure the required level of input beam pointing stability
- beam dumps and stray light baffles in the IO section of the vacuum system

## 5.4 Core optics

The scope of the core optic components subsystem includes:

- procurement of the following interferometer optics, including all coatings applied to them: test masses; end reaction masses; compensation plates; beamsplitter; fold mirrors; the large optics in the recycling cavities
- metrology of all core optics

- specification of cleaning procedures for core optics

The core optics design requirements are found in LIGO-T000127.

### 5.5 Suspensions

The suspensions subsystem includes:

- suspension mechanics for all core optics, for the small optics in the recycling cavities, for the input mode cleaner optics, and for the output mode cleaner
- local sensors, actuators and controls for local damping of these suspensions
- actuators and actuator-drivers for global control of suspended optics

The suspensions design requirements are found in LIGO-T010007.

### 5.6 Interferometer sensing & control

The interferometer sensing and control (ISC) subsystem includes:

- design of the interferometer sensing scheme
- sensors and controls for maintaining the interferometer lengths and alignment during operation
- sensors and controls for stabilizing the length and alignment of the input mode cleaner
- interferometer lock acquisition: hardware and/or algorithms for achieving the operating point of the interferometer
- signal sources for modulation frequencies used in the sensing scheme
- the in-vacuum optics platform and any seismic isolation of the platform for the input HAM chamber (HAM1/HAM7)
- any outside-the-vacuum mounting platforms for ISC hardware

The ISC design requirements are found in LIGO-T070236.

### 5.7 Auxiliary optics support

The auxiliary optics support (AOS) subsystem includes:

- Initial Alignment System: surveying support for proper installation of components
- Photon calibrators: calibration tool using photon pressure of a modulated laser beam

- Viewports for beams entering and exiting vacuum
- Optical levers to monitor orientation of suspended optics relative to the floor
- In-vacuum stray light control: baffles and beam dumps for diffuse scattering and ghost beams
- Beam reducing telescopes: for pick-off beams and ETM transmission beams
- Faraday isolator (in-vacuum) for the anti-symmetric port output beam
- Thermal compensation system: senses thermal distortions of core optics and corrects by adding compensating heat
- Video cameras for monitoring beam positions and sizes on the core optics

Requirements for the various components of AOS are documented separately, and several are still to be generated:

| | |
|---|---|
| Photon calibrator requirements | T070125 |
| Thermal compensation system (TCS) requirements | T000092 |
| Stray light control requirements | T070061 |

### 5.8 Control and data system

The control and data systems infrastructure includes:

- Data Acquisition (DAQ) System
- Timing and Synchronization System
- Computer Networking Systems
- Control room computer systems
- Diagnostic Monitoring Tool (DMT) computers

The control and data systems (CDS) infrastructure requirements are fount in LIGO-T070056.

## 6 Open system design issues

Here we summarize the open systems design issues and choices. These either involve multiple subsystems, or (predominantly) one subsystem but have a direct impact on detector performance.

- Test mass suspension fiber geometry (ribbon vs. stepped circular design).
- Test mass dielectric coating design (layer thicknesses).

- Gold coating on the test mass barrel.
- Mitigation for parametric instabilities.
- Electro-static charge mitigation.
- Arm length stabilization scheme.
- System for ensuring particulate cleanliness.

# A Appendix: Quantum Noise with Loss

Since the inclusion of losses in Bench's quantum noise calculation is relatively recent, we show in Fig. 9 the effect of different loss values on the quantum noise.

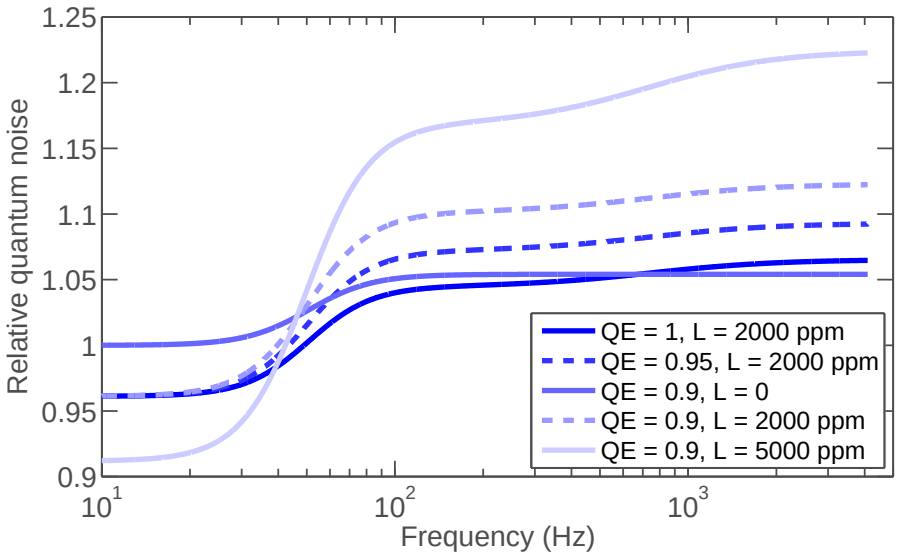


Figure 9: Quantum noise relative to the loss-less case (unity quantum efficiency and zero loss (L) in the signal recycling cavity). These curves are for the non-detuned, high-power case (mode 1b). We adopt nominal values of $QE = 0.9$ and $L = 2000\,ppm$.

# References

[1] *Advanced LIGO Project Execution Plan*, LIGO-M050303-03.

[2] *Advanced LIGO Reference Design*, LIGO-M060056-10.

[3] *LIGO Science Requirements Document (SRD)*, LIGO-E950018-02.

[4] *Strain Calibration in LIGO*, D. Sigg, LIGO-T970101-B.

[5] *Stable Recycling Cavity Mirror Coordinates And Recycling Cavity Lengths*, M. Smith, LIGO-T080078 (look for latest version).

[6] *Core Optics Components Preliminary Design*, LIGO-E080033.

[7] *DC Readout for Advanced LIGO*, P. Fritschel, LIGO-G030460-00.

[8] *Quantum noise in laser-interferometer gravitational-wave detectors with a heterodyne readout scheme*, A. Buonanno, Y. Chen, N. Mavalvala, Phys.Rev. D67 (2003) 122005.

[9] *DC Readout Experiment at the Caltech 40m Laboratory*, R. Ward, LIGO-G070447-00.

[10] `http://ilog.ligo-wa.caltech.edu:7285/advligo/Test_Mass_Beam_Sizes`

[11] *Optical torques in suspended Fabry-Perot interferometers*, J. Sidles and D. Sigg, Phys. Lett. A, 354 (2006) 167.

[12] *Arm Cavity Finesse for Advanced LIGO*, P. Fritschel, R.Adhikari, S. Ballmer, M. Evans, `http://www.ligo.caltech.edu/docs/T/T070303-01.pdf`

[13] *Advanced LIGO Substrate Selection Recommendation*, `http://www.ligo.caltech.edu/docs/M/M040405-00/M040405-00.pdf`

[14] *Test Mass Material Down-select Plan*, `http://www.ligo.caltech.edu/docs/T/T020103-08.pdf`

[15] *Dimensions for Advanced LIGO Fused Silica Test Masses*, P. Fritschel, `http://www.ligo.caltech.edu/docs/T/T040199-00.pdf`

[16] *Optimal degeneracy for the signal-recycling cavity in Advanced LIGO*, Yi Pan, `http://arxiv.org/pdf/gr-qc/0608128`.

[17] *HAM Seismic Isolation Requirements*, P. Fritschel, `http://www.ligo.caltech.edu/docs/T/T060075-00.pdf`

[18] textitHAM Single-Stage Isolation Baseline Option Review Report, F. Raab, `http://www.ligo.caltech.edu/docs/M/M060062-00/M060062-00.pdf`

[19] *Parametric oscillatory instability in FabryPerot interferometer*, V. B. Braginksy, S. Strigin, and S. Vyatchanin, Phys. Lett. A 287, 331 (2001).

[20] *Parametric Instabilities and Their Control in Advanced Interferometer Gravitational-Wave Detectors*, C. Zhao et al., Phys. Rev. Lett. 94, 121102 (2005).

[21] *Multiple modes contributions to parametric instabilities in advanced laser interferometer gravitational wave detectors*, L. Ju et al., Phys. Lett. A 354, 360 (2006).

[22] *Investigating a Parametric Instability in the LIGO Test Masses*, H. Bantilan and W. Kells, `http://www.ligo.caltech.edu/docs/T/T060207-00/T060207-00.pdf`.

[23] *Ring Dampers and Gold Coatings*, C. Zhao, talk given at the March 2008 LSC meeting, Caltech, Pasadena, CA.

[24] `http://ilog.ligo-wa.caltech.edu:7285/advligo/Seismic_Platform_Interferometer`

[25] *Quantum noise in second generation, signal-recycled laser interferometric gravitational-wave detectors*, A. Buonanno and Y. Chen, Phys.Rev. D64 (2001) 042006.

[26] *Thermoelastic Noise and Homogeneous Thermal Noise in Finite Sized Gravitational-Wave Test Masses*, Y. Liu, K. Thorne, Phys.Rev. D62 (2000) 122002.

[27] *Frequency and Surface Dependence of the Mechanical Loss in Fused Silica*, S. Penn et al., Phys. Lett. A 352 (2006) 3.

[28] *Optical coatings for gravitational-wave detection*, G. M. Harry et al., Proceedings of SPIE: 5578 (SPIE, Bellingham, WA, 2004).

[29] *Thermoelastic dissipation in inhomogeneous media: loss measurements and displacement noise in coated test masses for interferometric gravitational wave detectors*, M. Fejer et al., Phys. Rev. D 70, (2004) 082003.

[30] , M. L. Gorodetsky, and S. P. Vyatchanin, Physics Letters A 271 (2000) 303.

[31] *Optimized multilayer dielectric mirror coatings for gravitational wave interferometers*, J. Agresti et al., Proceedings of the SPIE, Volume 6286, pp. 628608 (2006).

[32] *Advanced LIGO Suspension System Conceptual Design*, N. Robertson et al., `http://www.ligo.caltech.edu/docs/T/T010103-05.pdf`.

[33] *Dissipation of mechanical energy in fused silica fibers*, A. Gretarrson and G. Harry, Rev. Sci. Instrum. 70 (1999) 4081.

[34] *Development of Fused Silica Suspensions for Advanced Gravitational Wave Detectors*, A. Heptonstall, talk given at the March 2008 LSC meeting, Caltech, Pasadena, CA.

[35] *Seismic gravity-gradient noise in interferometric gravitational-wave detectors*, S. Hughes, K. Thorne, Phys. Rev. D 58 (1998) 122002.

[36] *Measurement of Optical Path Fluctuations due to Residual Gas in the LIGO 40 Meter Interferometer*, M. Zucker, S. Whitcomb, `http://www.ligo.caltech.edu/docs/P/P940008-00.pdf`.